Defects in paramagnetic Co-doped ZnO films studied by transmission electron microscopy

A. Kovács,[1,a)] A. Ney,[2] M. Duchamp,[1] V. Ney,[2] C. B. Boothroyd,[1] P. L. Galindo,[3] T. C. Kaspar,[4] S. A. Chambers,[4] and R. E. Dunin-Borkowski[1]
[1]*Ernst Ruska-Centre for Microscopy and Spectroscopy with Electrons and Peter Grünberg Institute, Forschungszentrum Jülich, 52425 Jülich, Germany*
[2]*Institut für Halbleiter- und Festkörperphysik, Johannes Kepler Universität, Altenberger Str. 69, 4040 Linz, Austria*
[3]*Departamento de Ingeniería Informática, Universidad de Cádiz, 11510 Cádiz, Spain*
[4]*Fundamental and Computational Sciences Directorate, Pacific Northwest National Laboratory, Richland, Washington 99354, USA*

(Received 24 September 2013; accepted 4 December 2013; published online 23 December 2013)

We study planar defects in epitaxial Co:ZnO dilute magnetic semiconductor thin films deposited on *c*-plane sapphire (Al_2O_3), as well as the Co:ZnO/Al_2O_3 interface, using aberration-corrected transmission electron microscopy and electron energy-loss spectroscopy. Co:ZnO samples that were deposited using pulsed laser deposition and reactive magnetron sputtering are both found to contain extrinsic stacking faults, incoherent interface structures, and compositional variations within the first 3–4 Co:ZnO layers next to the Al_2O_3 substrate. The stacking fault density is in the range of 10^{17} cm^{-3}. We also measure the local lattice distortions around the stacking faults. It is shown that despite the relatively high density of planar defects, lattice distortions, and small compositional variation, the Co:ZnO films retain paramagnetic properties. © *2013 AIP Publishing LLC*. [http://dx.doi.org/10.1063/1.4851015]

I. INTRODUCTION

The prospect of combining ferromagnetic and semiconducting properties[1] is attractive for the design of spin-electronic devices, whose magnetic and transport properties can be controlled by the introduction of transition metal ions into a semiconducting host. Of the different doped oxides[2] that have been investigated as diluted magnetic semiconductors (DMSs), Co-doped ZnO (Co:ZnO) thin films, and nanostructures are among the most intensely studied materials because of the promising electronic and optical properties of the ZnO host material. A high Curie transition temperature (T_c) was predicted for transition-metal-doped zinc oxide by Dietl[3] *et al.* using a Zener type p-d exchange interaction model based on high concentrations of localized spins and delocalized free carriers (holes). At the same time, Sato and Katayama-Yoshida[4] used an *ab initio* local density approximation to predict that doping ZnO with Mn should lead to a ferromagnetic ground state in the presence of hole doping, but that Co, V, Cr, and Fe doping should show ferromagnetic ordering without additional carrier doping. These theoretical predictions were followed by contradictory experimental activities that either proved or disproved the existence of a high T_c in Co:ZnO.

In the last few years, however, there has been an emerging consensus of theoretical and experimental investigations showing that epitaxial Co:ZnO thin films with high crystalline quality are intrinsically paramagnetic,[5] with antiferromagnetic Co-O-Co interactions.[6,7] Recently, we have correlated the observed ferromagnetism in ZnO with the presence of secondary Co-rich phases.[8] These conclusions about the intrinsic magnetic properties of Co:ZnO relied on avoiding measurement artefacts when performing very sensitive superconductive quantum interference device (SQUID) magnetometry[9] in combination with synchrotron-based x-ray absorption spectroscopy (XAS), x-ray linear dichroism (XLD), and x-ray magnetic circular dichroism (XMCD).[5] The detection of small quantities of local structural or chemical variations using these techniques poses a significant analytical challenge and is ideally complemented by the application of advanced transmission electron microscopy (TEM) techniques to the same materials.[5,8] The need for high-spatial resolution studies of DMS materials, such as doped ZnO is even more important in view of the recent proposals that ferromagnetism in these materials may be related to the presence of structural defects.[10,11]

Here, we make use of recent advances in aberration-corrected TEM and optimized specimen preparation techniques for TEM to study the structure and chemistry of Co:ZnO layers that have been deposited onto *c*-plane sapphire using two common preparation techniques: pulsed laser deposition (PLD) and reactive magnetron sputtering (RMS). We use a combination of scanning TEM (STEM) imaging and electron energy-loss spectroscopy (EELS) to characterize grain boundaries, planar defects and interfaces in order to reveal structural features and possible chemical inhomogeneities, some of which have not been previously reported in transition-metal-doped oxides. We demonstrate that the presence of extended defects, which can be distinguished from simple point defects,[12] as well as non-stoichiometric layers of Co:ZnO, should be considered in realistic models of such DMS layers.

a)Author to whom correspondence should be addressed. Electronic mail: a.kovacs@fz-juelich.de

II. EXPERIMENTAL DETAILS

Thin epitaxial films of Co:ZnO were deposited onto *c*-plane sapphire substrates using PLD[13,14] and RMS.[5] Careful pre-characterization using x-ray diffraction, XAS, XLD, XMCD, and SQUID has been performed before for the PLD-10 (Refs. 5, 13, and 15) and RMS-10 (Ref. 15) samples, respectively, which has revealed that the samples are virtually phase pure and paramagnetic. These measurements suggest that Co occupies predominantly Zn lattice sites and is therefore likely to be in its formal 2+ oxidation state, i.e., that the samples are devoid of metallic Co precipitates. In addition, it has been found that in both samples the single ion anisotropy $D(S_z)^2$, which is induced by the anisotropic crystal field, is reduced to $D/k_B = 3\,K$, as compared to the bulk value of 4 K reported for impurities in single crystals.[15] In the present study, the two Co:ZnO samples with nominal $Co_xZn_{1-x}O$ compositions of $x = 0.10$ grown by RMS and PLD are complemented with another RMS sample with $x = 0.20$ (Table I) and all three were studied in cross-sectional geometry using TEM. The characterization of the RMS-20 sample using XAS, XLD, XMCD, and SQUID has also revealed that this sample is phase pure and paramagnetic and these findings will be published in Ref. 16.

TEM specimens were prepared using either conventional preparation (mechanical polishing followed by broad-beam ion milling) or focused ion beam (FIB) milling. In both cases, the specimens were finished using low-energy Ar ion milling at 500 eV, in order to remove ion-beam-induced artefacts. Image and probe aberration-corrected TEM and STEM studies were carried out at 300 keV using FEI Titan 80–300 microscopes, each of which is equipped with a double-hexapole corrector and a Gatan imaging energy filter. TEM and STEM images were recorded using a Gatan $2\,k \times 2\,k$ charge-coupled device camera and a Fischione 3000 detector, respectively. Strain maps were calculated from high-resolution TEM images using geometrical phase analysis[17] (GPA).

III. RESULTS AND DISCUSSION

TEM studies involved the characterization of grain boundaries and planar defects in the Co:ZnO layers, as well as the interface between each Co:ZnO layer and its *c*-plane sapphire substrate. Figure 1 summarizes the representative structural features in the Co:ZnO samples. All of the samples exhibit good epitaxy with the sapphire substrate, with a columnar but highly oriented grain structure that results from the presence of a large (~18%) lattice mismatch between *c*-plane sapphire and the *c*-plane of Co:ZnO. The Co doping of ZnO does not change significantly the growth process, thus a 30° rotation of Co:ZnO basal planes is expected with respect to the sapphire.[14] A strain field on both sides of the interface can be seen in a dark-field (DF) TEM image of the RMS-10 sample shown in Fig. 1(a), recorded using the 002 reflections of Co:ZnO and Al_2O_3. A detailed analysis of TEM images recorded from all three samples reveals that the grain diameters of the columns parallel to the substrate surface normal in the RMS-deposited and PLD-deposited layers are in the ranges 10 nm to 90 nm and 50 nm to 100 nm, respectively, as summarized in Table I. Figure 1(b) shows a high-resolution aberration-corrected high-angle annular DF (HAADF) STEM image of a 15 nm wide Co:ZnO grain in the RMS-10 sample. This grain is aligned along [010], while the two adjacent grains have different in-plane directions. The three grains that are visible in Fig. 1(b) exhibit a perfect match of their respective (002) planes with no additional phase visible at the grain boundaries. The interface between the Co:ZnO is abrupt. Interestingly, misfit dislocations are rarely observed in Co:ZnO, probably the strain is accommodated by the grain boundaries. The epitaxial relationship between the Co:ZnO layers and sapphire is determined as $Co:ZnO[010](001)//Al_2O_3[1\bar{1}00](001)$. Chemical composition measurements (not shown), acquired using energy dispersive X-ray spectroscopy from the PLD and RMS-10 samples, revealed homogenous chemical compositions of Co, Zn, and O across the grain boundaries. Figure 1(c) shows an aberration-corrected high-resolution TEM image of nanometer-sized planar defects (stacking faults) in the PLD-deposited sample (circles), which may be responsible for some of the local contrast variations that are visible within the

TABLE I. Properties of the paramagnetic RMS-deposited and PLD-deposited Co:ZnO layers on *c*-plane Al_2O_3 studied here.

	Co [at. %]	Layer thickness [nm]	Grain size [nm]	Stacking fault density [cm^{-3}]
RMS-10	10	158	15–90	2×10^{17}
RMS-20	20	128	10–50	6×10^{17}
PLD	10	113	50–100	3×10^{17}

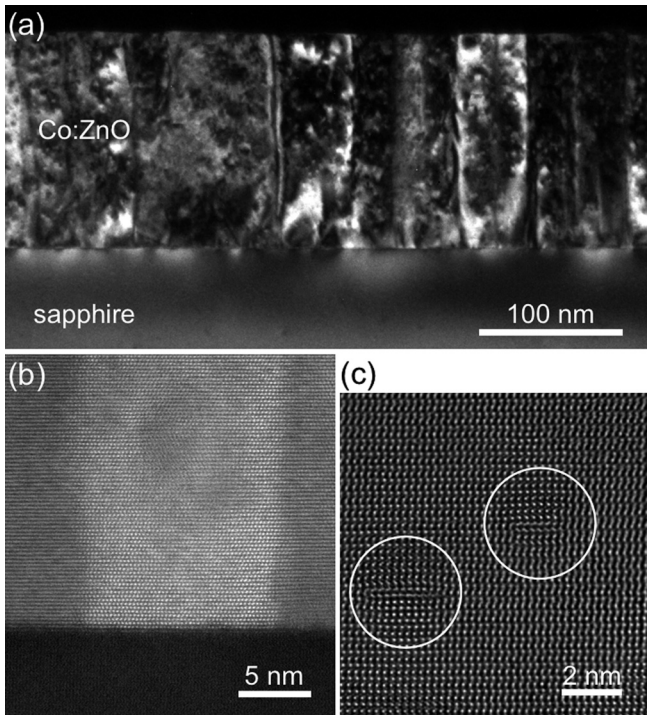

FIG. 1. (a) DF TEM image of sample RMS-10, recorded using 002 reflections of Co:ZnO and Al_2O_3. Some of the contrast variations at the interface and within the grains are due to strain. (b) HAADF STEM image of grain boundaries in sample RMS-10. The inner ADF detector semi-angle used was 48 mrad. (c) Aberration-corrected high-resolution TEM image of planar defects (marked using circles) in the PLD-deposited sample.

grains in Fig. 1(a). The typical length of each extra lattice plane in the Co:ZnO is ~2.5 nm in the PLD-deposited sample and ~5 nm in the RMS-deposited samples (see below). By estimating the thickness of the studied region using EELS and counting the stacking faults on high-resolution TEM images, the density is estimated as $2 \times 10^{17}\,\mathrm{cm}^{-1}$, $6 \times 10^{17}\,\mathrm{cm}^{-1}$, and $3 \times 10^{17}\,\mathrm{cm}^{-1}$ in RMS-10, RMS-20, and PLD samples, respectively (Table I). The error in the measured stacking fault density is expected to be ~20%.

The structures of the stacking faults and their local environments were studied in detail in sample RMS-10, as shown in Fig. 2. Figure 2(a) shows a high-resolution aberration-corrected TEM image of a stacking fault in this sample. The negative spherical-aberration imaging[18] (NCSI) technique was used to enhance the contrast of the atomic columns in the image. Aberration coefficients were corrected up to fourth order, with the negative spherical aberration coefficient (C_s) set to ~−10 μm and the objective lens defocus set to ~+10 nm to optimize the imaging conditions. The ~4-nm-long additional plane distorts the surrounding Co:ZnO lattice. The resulting strain distribution was visualized using GPA, as shown in Fig. 2(b). Surprisingly, the strain map was found to be affected strongly by the defocus used to record the image. Therefore, an exit wave function reconstruction was obtained from a defocus series of TEM images and the resulting phase component was used for the strain calculations. The resulting strain map, which is shown in Fig. 2(b), demonstrates that the lattice distortion is greatest around the partial dislocation cores of the stacking fault, with semi-circular regions that are in tension above and below the stacking fault, extending by ~5 nm into the lattice.

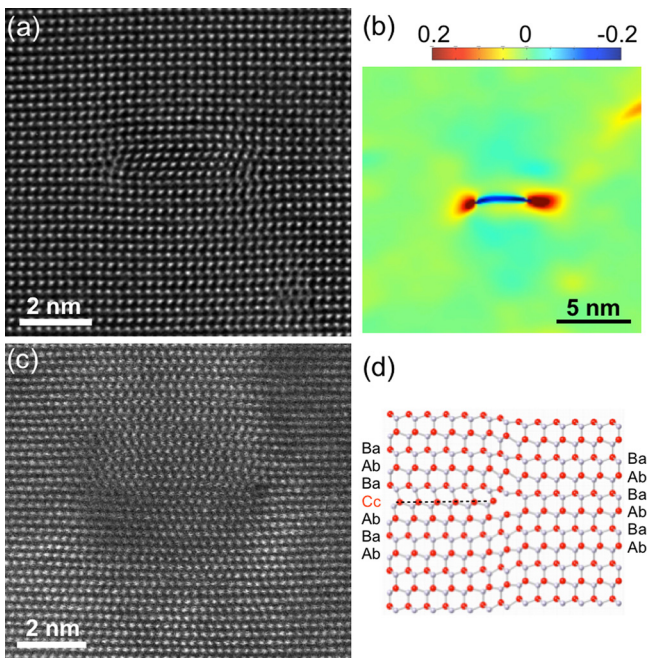

FIG. 2. Aberration-corrected (a) TEM and (c) STEM images of extrinsic stacking faults in the sample RMS-10. (b) Strain map (e_{yy} component) of the stacking fault shown in (a), calculated from the phase component of an exit-wave function reconstruction (not shown). Red = tension, blue = compression. (d) Structure model showing a possible core-structure containing a 5/7 ring. Grey = Zn(Co), red = O.

Figure 2(c) shows a high-resolution HAADF STEM image of a similar stacking fault, in which the bright spots correspond to Zn(Co) columns. Such defects were determined to be basal plane extrinsic stacking faults, with Frank partial dislocations and displacement vectors of $^1/_2$[001]. By matching the locations of the Zn(Co) atomic columns in the HAADF STEM image with a wurtzite structure model, a possible core structure of the stacking fault was determined, as shown in Fig. 2(d). The model suggests that the atomic columns in the core regions form tetragonally coordinated 5/7 rings,[19] with strongly distorted bond angles and lengths. Such stacking faults, with their associated strain distributions, are expected to affect carrier localization and local transport properties around the defects, according to first-principles total energy calculations.[20,21] Interestingly, these calculations also show that such extrinsic faults have high formation energies per unit cell compared to other intrinsic faults. Their presence in all three samples highlights the strongly off-equilibrium nature of both deposition techniques.

The interface structure between Co:ZnO and sapphire was also studied in more detail. Figure 3 shows an aberration-corrected high-resolution TEM image of the PLD sample viewed along the [1-100] direction of Al_2O_3. The image was recorded using the NCSI method, so that the Al and O columns in Al_2O_3 could be distinguished in the TEM image.[22] In Fig. 3(a), Al and Zn(Co) columns appear bright,

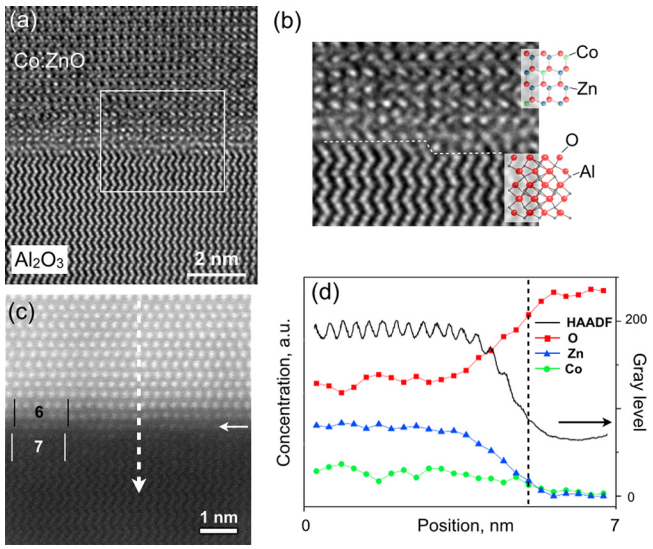

FIG. 3. (a) Aberration-corrected high resolution TEM image of the PLD sample acquired under NCSI conditions. The viewing direction is along [$1\bar{1}00$] of Al_2O_3. (b) Enlarged section of the marked area in (a), showing steps on the Al_2O_3 surface. The schematic representation of atomic columns includes Co atoms randomly placed on cation sites. (c) Atomic-resolution HAADF STEM image of the PLD sample viewed along the [1-100] Al_2O_3 direction. The inner ADF detector semi-angle used was 78 mrad. The interface is incoherent, with 6 planes of Co:ZnO matching 7 planes of Al_2O_3. The first Co:ZnO layer is marked by a white arrow. (d) HAADF and StripeSTEM measurements and the relative O, Zn, and Co concentrations extracted from the EELS results. The location of the first Co:ZnO layer is marked by vertical dotted line. The convergence angle of the electron beam was 25 mrad, while the collection angle of the spectrometer was ~25 mrad. The dispersion of the 2 k × 2 k camera was set up to be 0.5 eV/channel in order to record the core-loss O K (532 eV), Co L (709 eV), and Zn L (1020 eV) edges.

whereas O columns appear dark. The enlarged section of the interface shown in Fig. 3(b) reveals that the sapphire is O-terminated and that steps are present on the Al_2O_3 surface. Interpretation of the nature of the first Co:ZnO atomic layer is not straightforward, as the observed atomic structure does not represent the expected wurtzite structure, suggesting the presence of structural or chemical disorder in the first layer(s) of Co:ZnO. Figure 3(c) shows a high-resolution HAADF STEM image of the Co:ZnO-PLD layer viewed along $[1\bar{1}00]$ direction of the Al_2O_3 substrate. In the HAADF STEM image, the recorded intensity of the Co:ZnO film is higher than that of the Al_2O_3 substrate primarily due to the higher atomic numbers of Zn ($Z = 30$) and Co ($Z = 27$) compared to that of Al ($Z = 13$). The interface structure is incoherent, with 7 (110) Al_2O_3 planes matching 6 (100) Co:ZnO planes, as indicated in Fig. 3(c). The area shown in Fig. 3(c) does not contain any obvious steps or defects at the interface and appears to be structurally abrupt. However, the intensity of the Zn(Co) columns decreases close to the interface, which is suggestive of compositional variation or strain. Yu *et al.*[23] showed that the presence of strain at a SiO_2/Si interface causes a change in ADF STEM image intensity, which depends on inner detector semi-angle and specimen thickness. In the present specimens, the contrast of the Co:ZnO layers close to the interface in the ADF STEM image series was not observed to reverse as a function of collection angle over the range 20 to 120 mrad. It is therefore likely that a compositional variation is present in the Co:ZnO layers, probably dominated by a change in the relative concentration of Zn. In order to clarify the origin of the observed contrast, elemental analysis using the StripeSTEM[24] EELS technique was performed across the interface for O, Co, and Zn core-loss EELS edges. In this technique, an isochronous recording of EEL spectra and HAADF images provides spectroscopic information from individual atomic layers using an optimized irradiation dose.[25] Figure 3(d) displays measurements of elemental concentration profiles for O, Co, and Zn. Al was not included in the present measurement. The Zn concentration (upward pointing blue triangles in Fig. 3(d)) decreases faster compared to the Co concentration, while approaching the interface. At the same time, the O concentration increases towards the interface, suggesting the formation of a Co-containing interface layer, which is deficient in Zn. This conclusion is consistent with the observed decrease in HAADF STEM intensity in Fig. 3(c).

The compositional variation at the interface was also studied in detail in sample RMS-20, which contains the highest Co concentration of the three samples. Figure 4 shows an atomic-resolution HAADF STEM image and background-subtracted EELS measurements acquired across the interface between the Co:ZnO layer and the substrate viewed along the $[11\bar{2}0]$ direction of the Al_2O_3. Schematic ball-and-stick models of the Co:ZnO and Al_2O_3 structures are inserted for illustrative purposes. The presence of a monoatomic step on the Al_2O_3 surface is highlighted by a dotted line in Fig. 4(a). The contrast of the Zn(Co) columns decreases close to the interface in a similar manner to that found in the PLD sample in Fig. 3.

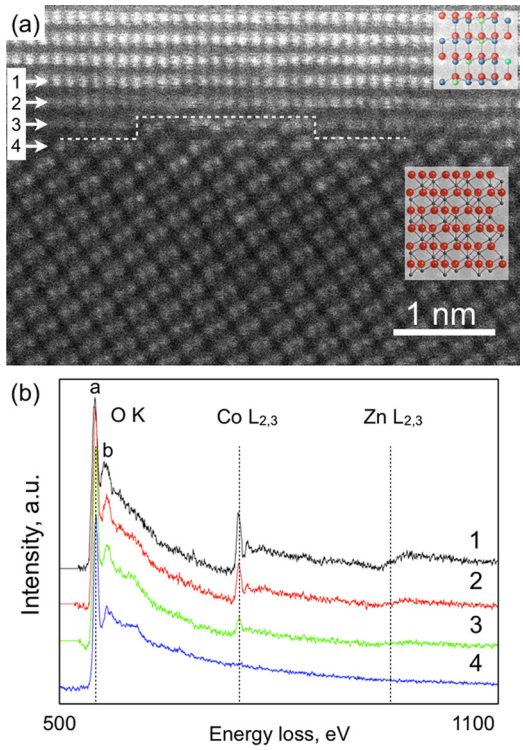

FIG. 4. (a) HAADF STEM image of the sample RMS-20 viewed along the $[11\bar{2}0]$ direction of Al_2O_3. The inner ADF detector semi-angle used was 78 mrad. The insets show schematic models of the crystal structures (red = O, blue = Zn, green = Co, dark grey = Al). The dotted line at the interface marks a monoatomic step on the Al_2O_3 surface. (b) Representative background-subtracted EELS spectra showing the O K, Co $L_{2,3}$, and Zn $L_{2,3}$ edges acquired across the interface at the positions marked in (a).

Figure 4(b) shows EEL spectra recorded from the first four Co:ZnO monolayers by scanning the electron beam along a ~5 nm length parallel to the interface and integrating the EELS signal. The signal-to-noise ratio in the individual spectra was improved by applying principal component analysis using custom-written software. Spectrum 1 in Fig. 4(b), which is the furthest measurement from the interface, shows well-defined O, Co, and Zn peaks. Spectrum 3 was recorded from the atomic layer with the step, i.e., from both Co:ZnO and sapphire, accounting for the reduced intensity of the Co and Zn peaks. The Zn peak intensity decreases in spectrum 2 as the interface is approached. The measurements support the formation of a Zn-deficient layer within the first 2–3 atomic layers between the sapphire substrate and the Co:ZnO.

In Fig. 4(b), the sharp Co L_3 and L_2 peaks at 780 and 800 eV correspond to transitions from 2p core states to bound unoccupied 3d states, which hybridize with oxygen 2p orbitals in oxides and can be used to measure changes[26,27] in transition metal valency or oxidation state. Figure 5 shows measured values of Co L_3/L_2 ratios, plotted alongside ratios of the first and second O K-edge peaks appearing at ~532 eV and 550 eV (marked as "a" and "b"). The inset in Fig. 5(a) shows an HAADF STEM image recorded during StripeSTEM EELS acquisition with successive monolayers marked 1 to 12, where the Co:ZnO layer closest to the substrate is number 12. The L_3/L_2 ratio was determined by using a standard fitting procedure that includes background

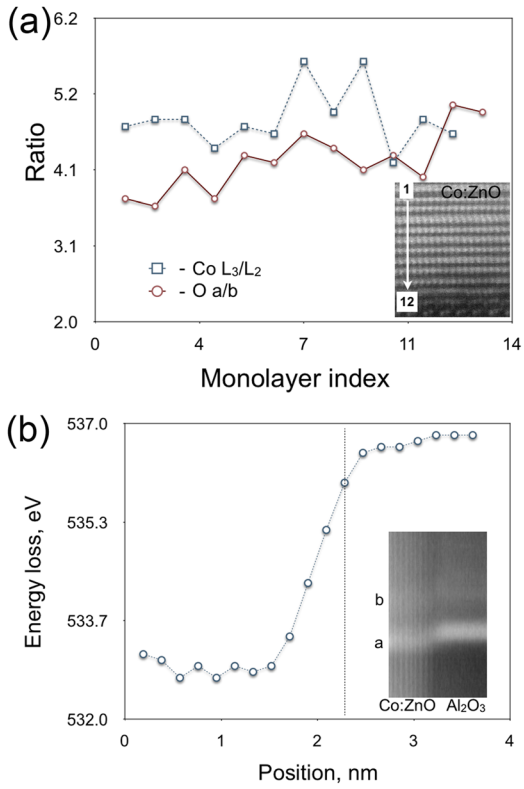

FIG. 5. (a) Co L_3/L_2 edge ratios and O a/b edge ratios determined for the first 12 layers (13 for O) of Co:ZnO sample (RMS-20) determined from the StripeSTEM EELS measurement shown in Fig. 4. The inset shows an HAADF image recorded during the acquisition. The scan direction and the numbers of the layers are marked. (b) Chemical shift of the O K edge measured across the interface. Vertical line indicates the interface. The inset shows the original O K edge EELS spectra, displayed with a size of 3 nm × 48 eV.

subtraction using a power law, calculation of the Hartree-Slater ionization cross-section to fit the continuum and the use of gaussian functions to fit the extracted L_3 and L_2 peaks. The total relative error of the measured ratios was estimated to be ~10% due to the relatively low signal-to-noise ratios of the measurements. Taking this uncertainty into consideration, Fig. 5(a) indicates that the oxidation state of Co does not vary significantly across the first 12 layers of the Co:ZnO film. The average L_3/L_2 ratio is determined to be 4.8, which is close to that of CoO (~5), which has a similar coordination number. The oxidation state of Co is therefore inferred to be 2+ in Co:ZnO,[28] in agreement with our X-ray absorption measurements, suggesting that Co substitutes for Zn in the lattice uniformly.[13]

Figure 5(a) shows that the O a/b ratio increases slightly on approaching the interface between the Co:ZnO layer and the Al_2O_3. Since these measurements have relatively large errors, a more sensitive approach was used involving measurements of the threshold energy of the O K-edge to follow the change in chemical environment across the interface, as shown in Fig. 5(b). The main O K-edge peak was fitted using a gaussian function and its onset energy was plotted, as shown in Fig. 5(b). In the Co:ZnO, the O edge is measured to be at ~532 eV. However, a chemical shift of ~4 eV is observed for O in Al_2O_3. This chemical shift is not abrupt, but changes in position gradually within the first 4 layers in the Co:ZnO film. Such a shift may be induced by a change in Zn/Co concentration in the first monolayers of Co:ZnO. However, these data should be considered as preliminary and treated with caution, because the insulating Al_2O_3 can introduce an energy bandgap close to the interface, increasing the ionization threshold energy[29] and giving rise to a more complex chemical interface structure. Future simulation of the electronic structure of the interface will help provide more insight on this phenomenon. A similar chemical shift was not observed for the Co $L_{2,3}$ edge, corroborating the results of the analysis of the peak ratio in Fig. 5(a), which suggest that there is no change in Co valence. The interface structure of the PLD sample was studied in a similar manner to the analysis of the RMS-20 sample presented in Fig. 5. The same values were obtained for the chemical shift of O and its absence for Co. The first Co:ZnO monolayer was again grown on a step-mediated Al_2O_3 surface.

Taking together the decrease in ADF STEM intensity, the decrease in Zn concentration measured using EELS and the chemical shift of the O edge suggest that the first monolayers of Co:ZnO are deficient in Zn, while the Co oxidation state remains essentially 2+.

IV. SUMMARY

We have used advanced TEM and EELS methods to study the structure and chemistry of grain boundaries and plate-like stacking faults in three Co:ZnO samples, as well as the interface between the Co:ZnO films and their sapphire substrate. Thin films of Co:ZnO with Co concentrations of 10% and 20% are deposited on sapphire substrates using RMS and PLD methods. The TEM characterization confirms the high crystalline quality of the films, thus no formation of secondary phases or precipitates is detected. Since all three samples are known to be paramagnetic, the presence of the defects cannot be associated with magnetic order, as speculated previously.[11] The extrinsic stacking faults that are present in each Co:ZnO layer introduce regions of both compressive and tensile strain into the wurtzite structure. The stacking fault densities in the RMS and PLD deposited films are in the $10^{17}\,cm^{-3}$ range (Table I). The presence of the observed lattice distortions may be responsible for the reduction of the single ion anisotropy D, which was reported before for the RMS-10 and PLD-10 samples.[15]

The chemical compositions and electronic structures of the first few monolayers of Co:ZnO adjacent to the Al_2O_3 substrate were also studied. In each sample, the interface is incoherent but atomically abrupt. Variations in chemical composition are found only in the first 2–4 layers in the Co:ZnO film, which are Zn-deficient. In these first few layers, the Co appears to remain in its 2+ valence state. These findings are supportive of the formation of an interfacial layer, which facilitates subsequent growth of the polar *c*-oriented wurtzite ZnO structure.

ACKNOWLEDGMENTS

The authors would like to thank D. Meertens (Forschungszentrum Jülich, PGI-5) for the preparation of FIB

lamellas, and M. Luysberg, L. Houben (Forschungszentrum Jülich, PGI-5), I. Maclaren (University of Glasgow), and M. S. Moreno (Bariloche, Argentina) for useful comments related to this study. T.C.K. and S.A.C. were supported by the U.S. Department of Energy (DOE), Office of Science, Office of Basic Energy Sciences, Division of Materials Sciences and Engineering. Film growth by PLD was performed using EMSL, a national scientific user facility sponsored by the U.S. DOE's Office of Biological and Environmental Research, located at the Pacific Northwest National Laboratory (PNNL). M.D. acknowledges financial support from the European Union under a contract for an Integrated Infrastructure Initiative 312483 – ESTEEM2.

[1]T. Dietl, Nature Mater. **9**, 965 (2010).
[2]J. M. D. Coey and S. A. Chambers, MRS Bull. **33**, 1053 (2008).
[3]T. Dietl, H. Ohno, F. Matsukura, J. Cibert, and D. Ferrand, Science **287**, 1019 (2000).
[4]K. Sato and H. Katayama-Yoshida, Jpn. J. Appl. Phys., Part 2 **39**, L555 (2000).
[5]A. Ney, M. Opel, T. C. Kaspar, V. Ney, S. Ye, K. Ollefs, T. Kammermeier, S. Bauer, K.-W. Nielsen, S. T. B. Goennenwein, M. H. Engelhard, S. Zhou, K. Potzger, J. Simon, W. Mader, S. M. Heald, J. C. Cezar, F. Wilhelm, A. Rogalev, R. Gross, and S. A. Chambers, New J. Phys. **12**, 013020 (2010).
[6]P. Sati, C. Deparis, C. Morhain, S. Schäfer, and A. Stepanov, Phys. Rev. Lett. **98**, 137204 (2007).
[7]A. Ney, V. Ney, F. Wilhelm, A. Rogalev, and K. Usadel, Phys. Rev. B **85**, 245202 (2012).
[8]A. Ney, A. Kovács, V. Ney, S. Ye, K. Ollefs, T. Kammermeier, F. Wilhelm, A. Rogalev, and R. E. Dunin-Borkowski, New J. Phys. **13**, 103001 (2011).
[9]M. Sawicki, W. Stefanowicz, and A. Ney, Semicond. Sci. Technol. **26**, 064006 (2011).
[10]J. M. D. Coey, P. Stamenov, R. D. Gunning, M. Venkatesan, and K. Paul, New J. Phys. **12**, 053025 (2010).
[11]B. B. Straumal, A. A. Mazilkin, S. G. Protasova, P. B. Straumal, A. A. Myatiev, G. Schütz, E. J. Goering, T. Tietze, and B. Baretsky, Philos. Mag. **93**, 1371 (2013).
[12]C. H. Patterson, Phys. Rev. B **74**, 144432 (2006).
[13]A. Ney, K. Ollefs, S. Ye, T. Kammermeier, V. Ney, T. C. Kaspar, S. A. Chambers, F. Wilhelm, and A. Rogalev, Phys. Rev. Lett. **100**, 157201 (2008).
[14]T. C. Kaspar, T. Droubay, S. M. Heald, P. Nachimuthu, C. M. Wang, V. Shutthanandan, C. A. Johnson, D. R. Gamelin, and S. A. Chambers. New J. Phys. **10**, 055010 (2008).
[15]A. Ney, T. Kammermeier, K. Ollefs, S. Ye, V. Ney, T. C. Kaspar, S. A. Chambers, F. Wilhelm, and A. Rogalev, Phys. Rev. B **81**, 054420 (2010).
[16]A. Ney, V. Ney, M. Kieschnick, F. Wilhelm, K. Ollefs, and A. Rogalev, "Structure, valence and magnetism of Co-doped ZnO at the coalescence limit," J. Appl. Phys. (to be published).
[17]M. J. Hytch, E. Snoeck, and R. Kilaas, Ultramicroscopy **74**, 131 (1998).
[18]C. L. Jia, L. Houben, A. Thust, and J. Barthel, Ultramicroscopy **110**, 500 (2010).
[19]P. Komninou, J. Kioseoglou, G. P. Dimitrakopulos, T. Kehagias, and T. Karakostas, Phys. Status Solidi A **202**, 2888 (2005).
[20]C. Stampfl and C. G. Van de Walle, Phys. Rev. B **57**, R15052 (1998).
[21]Y. Yan, G. M. Dalpian, M. M. Al-Jassim, and S.-H. Wei, Phys. Rev. B **70**, 193206 (2004).
[22]A. H. Heuer, C. L. Jia, and K. P. D. Lagerlöf, Science **330**, 1227 (2010).
[23]Z. Yu, D. A. Muller, and J. Silcox, J. Appl. Phys. **95**, 3362 (2004).
[24]M. Heidelmann, J. Barthel, and L. Houben, Ultramicroscopy **109**, 1447 (2009).
[25]L. Houben, M. Heidelmann, and F. Gunkel, Micron **43**, 532 (2012).
[26]Z. L. Wang, J. Bentley, and N. D. Evans, Micron **31**, 355 (2000).
[27]H. Tan, J. Veerbeck, A. Abakumov, and G. Van Tendeloo, Ultramicroscopy **116**, 24 (2012).
[28]M. S. Moreno, T. Kasama, R. E. Dunin-Borkowski, D. Cooper, P. A. Midgley, L. B. Steren, S. Duhalde, and M. F. Vignolo, J. Phys. D: Appl. Phys. **39**, 1739 (2006).
[29]L. A. Grunes, Phys. Rev. B **27**, 2111 (1983).